Control of interlayer temperature through laser power optimization in powder bed fusion

Yong Ren[1], Corey Dickman[2], Matthew Pantano[2], Edward Reutzel[2], and Qian Wang*[1]

[1]Department of Mechanical Engineering, The Pennsylvania State University, University Park, PA 16802

[2]Applied Research Laboratory, The Pennsylvania State University, University Park, PA 16802

Abstract

Existing studies have demonstrated that for laser powder bed fusion (L-PBF) processes, applying the default parameters given by the manufacturers to build certain geometries (e.g., those including an overhang structure) could lead to overheating during the build process. Therefore, there is a strong need to optimize process parameters over the geometry to reduce overheating. Prior studies have also shown that interlayer temperatures have a significant thermal effect on the resulting melt-pool size and morphology, suggesting the need of controlling part-level temperatures to improve the build quality. Motivated by these needs, this paper presents an experimental demonstration of a model-based optimal control of laser power on each grouped layer (consisting of multiple physical layers) to reduce interlayer temperatures below a target threshold. The optimal laser-power profiles are derived from solving a convex program, which

*Corresponding author, quw6@psu.edu

provides a theoretical guarantee for optimality, and they are implemented on an EOS M280 L-PBF system as a feed-forward control. Results from this study show that the thermal control is capable of reducing interlayer temperatures when needed. Moreover, the thermal control helps reduce the variability of melt-pool size along the build direction, leading to more than 20% reduction in melt-pool mean half-width at a representative layer (layer 876) compared to the uncontrolled case. Furthermore, the microhardness of the area of interest (near layer 876) under the thermal control has 6% increase in the percentage-of-test-points above 297 HV and 32% increase in the percentage-of-test-points above 318 HV compared to the uncontrolled case, indicating improved hardness under the optimal control of laser power.

keyword: Interlayer temperature; multi-input multi-output (MIMO); optimal control; part-scale thermal control; melt-pool morphology, microhardness

1 Introduction

Laser powder bed fusion (L-PBF) is an important metal-based additive manufacturing (AM) process that enables fabrication of complex parts with a high geometric resolution [1]. The default AM process parameters recommended by AM machine manufacturers are typically identified through experimental trial-and-error on a set of simple test coupons. However, such default parameter values often do not work well in building a more complex geometry. For example, overheating often occurs during the build process of an overhang structure, where more energy is used to scan each layer with the increase of the build height while there is insufficient conduction to dissipate heat away [2, 3]. Such overheating is often associated with poor build quality such as over-melting and keyhole-induced porosities [4, 5]. Therefore, there is a strong need to optimize process parameters over the geometry to avoid overheating.

Most of the existing efforts for process control to reduce overheating focused on scan-vector

level control to reduce local overheating within a layer [6–12]. A full simulation of scan-vector level control in finite-element (FE) analysis requires running a moving-source model and is computationally prohibitive for simulating a sizable part. Only a few studies investigated the layer-by-layer, part-level thermal control to reduce overheating [13–16], as reviewed in the following. In Ma et al. [13], when the surface defect area ratio, computed from in-situ images of part surface, fell below a predefined threshold at a layer, a proportional controller was applied to adjust laser power at subsequent layers to enhance surface quality in the L-PBF process. Vasileska et al. developed a closed-loop layer-wise control strategy for building large overhang parts [14]. A switching-logic controller with constant control gains was applied to reduce the laser duty cycle when the measured laser heated area was larger than its nominal value. However, their results were not validated with a porosity analysis despite that the reduced energy density could cause lack-of-fusion defects.

In Riensche et al. [15], a graph-theory based thermal model was used to determine the layers with potential heat buildup by checking if the simulated end-of-cycle surface temperature had more than 20 ^oC increase between two successive layers. Then, a trial-and-error iterative thermal simulation was performed with respect to the laser power and interlayer dwell time. In their experimental evaluation, only two laser power values (either the default 285 W or a lower-bound of the laser power) were used, together with applying a fixed 10 s interlayer dwell time when needed.

Kavas et al. [16] developed a linear-quadratic feedback controller of laser power to stabilize the interlayer temperatures for three overhangs of 45^o, 68^o, and 80^o in L-PBF. An empirical linear time-invariant model was obtained by applying system identification over collected data of laser powers and the resulting average layer temperatures on test prints. However, the system-identification model in [16] did not account for the fact that heat accumulation is geometric-dependent, causing large (60 ^oC) predication errors for the 45^o overhang.

It is worth pointing out that in both Riensche et al. [15] and Kavas et al. [16], *a single laser-power*

value was applied for each part layer that needed to be corrected. This worked well for parts with a simple geometry composed of a single geometric feature in each layer, where the temperature distribution of a layer was relatively uniform. However, for a complex geometry where a layer consists of multiple geometric features each of which has its own level of temperature, applying the same laser power value for the entire layer becomes problematic. For example, in order to correct the heat buildup in one region of a layer, the reduced laser power could cause lack-of-fusion in another region of the same layer. Consequently, applying an individualized level of laser power for each geometric feature in a layer is needed to tackle such complexity.

This paper presents an experimental demonstration of a model-based part-level optimization of laser power to reduce interlayer temperatures below a target threshold. Interlayer temperature is the layer temperature right before laser starting to melt a new powder layer [3,17–19]. It reflects the thermal accumulation from building the past layers, and thus it can serve as a proxy to indicate where overheating occurs and needs to be corrected. A square-canonical geometry is used as a demonstrating example. Its multiple geometric features (inner- or outer-wall, support structure) in a layer exhibit different interlayer temperatures and thus require different levels of laser power, e.g., one power value for the inner-wall and a different power value for the outer-wall.

The part-level optimization of laser power in this study is enabled by the finite-difference (FD) part-scale thermal model developed in our prior work [19]. The model defines a node for each geometric feature in a part slice and along the build direction, the nodes form a multi-branch network (see Sec. 2.2). Compared to conventional FD models defined on a regular grid [20, 21], this network-based FD model allows an easier way to handle curved or irregular geometries and it needs a much reduced number of nodes with decent modeling accuracy. As the FD model defines a node for each geometric feature in a part slice, it allows the development of an (FD) node-dependent laser power optimization that controls each geometric feature with an individualized

level of laser power. In addition to modeling development, our prior work [19] also included a preliminary control simulation with the purpose of showing the feasibility of using the model for thermal control, without any experimental evaluation. Built on top of the prior results in [19], this study focuses on improving build quality through the control of interlayer temperatures, by comparing two laser-power optimization schemes with and without imposing a practical lower bound on laser power. The experimental investigation in this study serves two purposes. First, our prior work [19] only validated the FD model under a constant laser power. It is unknown if the model would still hold under a range of varying laser power values, which is necessary for model-based process optimization. The experimental results in this study show that the model-based laser power optimization is able to enforce the interlayer temperature below a target threshold for most of the part layers. This implies that the FD model is able to capture the essential physics of the part-scale thermal evolution, albeit developed based on many assumptions and simplifications. Second, through evaluation of melt-pool cross-sections and microhardness at representative layers of as-built samples, the experimental investigation in this study shows that the proposed optimization of laser power with a lower power bound can reduce the variability of melt-pool size along the build direction and also improve the microhardness, indicating improvement of build quality under the optimal control of laser power.

The control optimization in this study makes the following contributions to the existing literature on part-level thermal control: 1) Providing the resulting control strategies with a theoretical guarantee of optimality. Compared to Riensche et al. [15], where the laser-power input was obtained through heuristics, this paper derives the laser-power profiles from solving a convex program; 2) Advancing the applicability of laser power optimization to more complex geometries. Compared to Kavas et al. [16], where the system-identification model ignored the geometric-dependent heat accumulation, the optimization in this paper solves upon a finite-difference model that captures

not only the part-geometry, but also the complex heat transfer among part components, support structures, and powder. Compared to the one-power-per-layer control in Riensche et al. [15] and Kavas et al. [16], this study optimizes (FD) node-dependent laser powers for different geometric features in a layer.

This paper is organized as follows. The methods and materials are given in Sec. 2, where we give a brief overview of the part-scale thermal model introduced in our prior work [19], followed by presenting two optimization schemes to control the interlayer temperatures. We then present the experimental setup for feed-forward control implementation of the optimized laser power profiles, in-situ thermal imaging, and micrograph and microhardness measurements of the final samples. Experimental results and discussions are given in Sec. 3, and conclusions are drawn in the end.

2 Methods and Materials

2.1 Part geometry

This study considers the same twin square-canonical geometry of Inconel 718 as in [22] (see Fig. 1). Each canonical part consists of 1270 layers with a dimension of 64.24 mm $\times$ 64.24 mm $\times$ 50.8 mm, built on a tool steel substrate of 252 mm $\times$ 252 mm $\times$ 30 mm by the EOS M280 L-PBF system. The part structure is composed of an outer wall and an inner wall, which are separated at lower layers, then merged at layer 1020 to form an overhanging junction, and eventually separated at layer 1144 till the end. The thickness of the outer wall is 2.29 mm, and the thickness of the inner wall is 0.83 mm at its lower layers. Porous support structures of Inconel 718 are used during the build process. They are in the form of square honeycombs with a wall spacing of 0.82 mm and a wall thickness of 0.12 mm. As illustrated in the mid-section view of the part in Fig. 1, the support starts to get contact with the inner wall surface at layer 894.

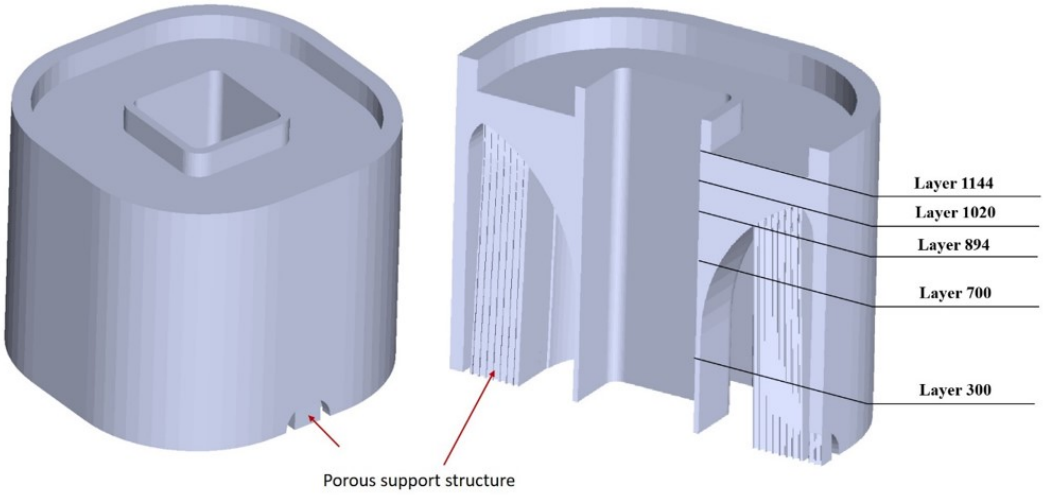

Figure 1: STL of the square-canonical geometry.

Each powder layer has a thickness of 40 μm. All scans have a hatch spacing of 110 μm. In order to compare and assess the melt-pool morphology along the build direction, the build plan is designed to align hatches in X and Y directions, with a 90^o rotation angle from layer to layer. Fig. 2 shows the hatch/stripe patterns from two sample layers. Such build plan allows alignment of melt-pool cross-sections from every other layers along the build direction (in Z-direction) after performing a XZ-plane cut to the as-built sample. The substrate is heated and maintained at 80 ^oC during the build process.

2.2 Overiew of a multi-branch-network based part-scale thermal model

Our prior work developed a multi-branch-network based part-scale thermal model using a finite difference method [19]. The model is established based on the following assumptions and simplifications: 1) It is assumed that the heating process of a whole layer of the powder bed by the laser beam is simultaneous and thus the hatch-by-hatch scanning strategies are not explicitly accounted; 2) A layer-scaling scheme is applied to utilize grouped layers (each consists of multiple physical

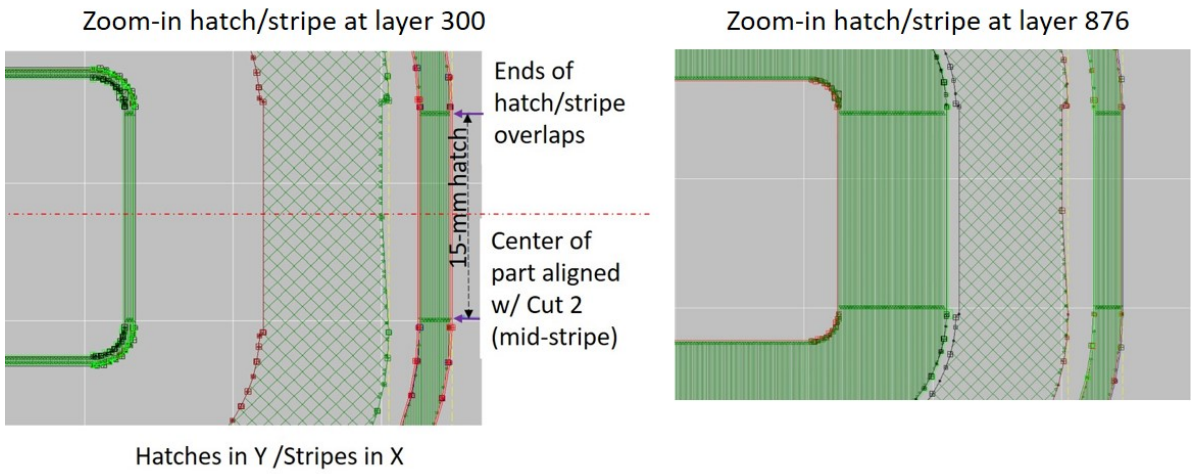

Figure 2: Hatch/stripe at two sample layers.

layers) in thermal modeling to reduce the overall model dimension; 3) Constant thermal properties are assumed and thermal radiation is omitted to simplify the process physics; and 4) It is assumed that for a part slice, the variance of temperature distribution of each geometric feature is small. The first assumption has been widely adopted in part-scale FE models [18, 23–29], the second assumption adopted in [28, 30–32], and the third assumption adopted in [15]. The fourth assumption is supported by the experimental observation from [3].

The square-canonical geometry is divided into a total of 70 grouped layers (part slices) with each consisting of 18 physical layers. For a grouped layer, one node is defined for the inner wall and one node is defined for the outer wall when the two walls are separated. If a grouped layer contains supports, an additional node is defined for each support. A substrate node is defined for each substrate slice. A network structure showing thermal conduction among the nodes is given in Appendix A. An aggregate powder node is also defined in each grouped layer. It is connected to all other nodes in the same grouped layer to characterize the heat loss from each fused solid component (part, support or substrate) to the powder, and it is also connected to the top/below

powder nodes in the neighboring grouped layers. The study in [19] shows that the powder nodes serve as a medium between the inner- and outer-wall and they play a critical role in modeling the thermal interaction between the inner- and outer-wall.

Consider a grouped layer ℓ. Let t_{tot}^{ℓ} denote the total simulation period for building layer ℓ, then $t_{tot}^{\ell} = t_{proc}^{\ell} + t_{recoat}^{\ell}$, where t_{proc}^{ℓ} and t_{recoat}^{ℓ} denote the respective laser processing time and recoating time. Further let T_i^p denote the temperature of each node i at a time increment p. Next, define the part-level temperature vector as follows:

$$\mathbf{T}_{\ell}^{p} \triangleq [T_1^p, \ldots, T_i^p, \ldots, T_{N_\ell}^p]^{\top} \tag{1}$$

where N_ℓ denotes the total number of nodes on and beneath layer ℓ.

Then, the part-level temperature field $\mathbf{T}_{\ell}^{p}$ is governed by the following FD model in a compact matrix form [19]:

$$\mathbf{T}_{\ell}^{p+1} = \mathbf{\Gamma}^{-1}(\mathbf{\Lambda}\mathbf{T}_{\ell}^{p} + \mathbf{R}T_a), \quad p = 0, \cdots, n_\ell - 1 \tag{2}$$

where T_a is the ambient temperature, and n_ℓ is the maximum time index for t_{tot}^{ℓ}. The matrices $\mathbf{\Gamma}$, $\mathbf{\Lambda}$, and $\mathbf{R}$ are given in Appendix A. The initial condition $\mathbf{T}_{\ell}^{0}$ is given as follows [19]:

$$(\mathbf{T}_{\ell}^{0})^{\top} = \left[(\mathbf{T}_{\ell-1}^{n_{(\ell-1)}})^{\top} \quad (\mathbf{T}_{act}^{\ell}(\mathbf{P}_\ell))^{\top}\right] \tag{3}$$

where $\mathbf{T}_{\ell-1}^{n_{(\ell-1)}}$ denotes the temperature vector at the final time index $n_{(\ell-1)}$ of the previous layer $(\ell-1)$; $\mathbf{T}_{act}^{\ell}$ denotes the activation temperature vector for the m_ℓ number of nodes on layer ℓ, and it is a function of the the laser power vector $\mathbf{P}_\ell$. The dimension of the laser power vector $\mathbf{P}_\ell$ is $m_\ell \times 1$, with each element $P_{\ell}^{(i)}$ denoting the laser power for node i in layer ℓ . The mathematical expression of $\mathbf{T}_{act}^{\ell}(\mathbf{P}_\ell)$ is given in Appendix A.

2.3 Optimal control of interlayer temperature

In terms of the dynamic equation (2) for the part-level temperature field, a variety of thermal control optimizations can be formulated to achieve different control objectives. This study focuses on optimal control of interlayer temperatures. In terms of the part-level temperature field $\mathbf{T}_\ell^p$, the interlayer temperature $\mathbf{T}_\ell^{inter}$ immediately before the laser melting a new layer $(\ell+1)$ can be derived as follows [19]:

$$\mathbf{T}_\ell^{inter} = \mathbf{S}\mathbf{T}_\ell^{n_\ell} \tag{4}$$

where $\mathbf{T}_\ell^{inter}$ is a vector of $m_\ell \times 1$, with m_ℓ denoting the number of nodes on layer ℓ; $\mathbf{S}$ is a matrix of $m_\ell \times N_\ell$,

$$\mathbf{S} = \begin{pmatrix} 0 & \cdots & \cdots & 0 & 0 & 1 \\ 0 & \cdots & \cdots & 0 & 1 & 0 \\ \vdots & \vdots & \vdots & \vdots & \vdots & \vdots \\ 0 & \cdots & 0 & 1 & \cdots & 0 \end{pmatrix} \tag{5}$$

with its elements $s(i,j) = 1$ if $i + j = N_\ell + 1$; $s(i,j) = 0$ otherwise.

For the square-canonical geometry, it is shown in [3] that under the default laser power of 285 W, the interlayer temperatures range from 80 ^oC to above 300 ^oC (see Sec. 3.1). The root-mean-square error between the model computed interlayer temperatures and mean values of the measured temperatures was less than 25 ^oC, and the corresponding mean error rate of the prediction was less than 11%.

Two optimal control formulations are considered in this study for experimental investigation. In the first formulation (*OPT1: Opt w/o power-bound*), the laser power is optimized, without a lower bound, such that the interlayer temperatures will not exceed a pre-specified target threshold value. A preliminary simulation of *OPT1* was explored in [19] without experimental validation. It is known that if the laser power is dropped too low, it will fail to melt the powder and lead

to lack-of-fusion defects. Hence, a lower bound for laser power is imposed in the second optimal control (*OPT2: Opt w/ lower-power-bound*).

For each grouped layer ℓ, the mathematical formulations of OPT1 and OPT2 are given as follows:

OPT1: Opt w/o power-bound :

$$\min_{\mathbf{P}_\ell} \quad J = \| \mathbf{P}_\ell - \mathbf{P}_{default} \|^2 \tag{6}$$

$$\begin{aligned} s.t. \quad & \mathbf{T}_\ell^{p+1} = \mathbf{\Gamma}^{-1}(\mathbf{\Lambda}\mathbf{T}_\ell^p + \mathbf{R}T_a), \quad p = 0, \cdots, n_\ell - 1 \\ & (\mathbf{T}_\ell^0)^\top = \left[(\mathbf{T}_{\ell-1}^{n_{(\ell-1)}})^\top \quad (\mathbf{T}_{act}(\mathbf{P}_\ell))^\top\right] \\ & \mathbf{T}_\ell^{inter} = \mathbf{S}\mathbf{T}_\ell^{n_\ell} \\ & \mathbf{T}_\ell^{inter} \leq \overline{\mathbf{T}}^{inter} \end{aligned} \tag{7}$$

OPT2: Opt w/ lower-power-bound :

$$\begin{aligned} \mathbf{OPT1} : eq.(6) \quad & - \quad eq.(7) \\ \mathbf{P}_\ell \quad & \geq \quad \underline{\mathbf{P}} \end{aligned} \tag{8}$$

where the cost function in eq. (6) drives the optimization to favor laser power values that are closest to the default value provided by the machine manufacturers. The inequality (7) imposes that the interlayer temperature should not exceed a target threshold $\overline{\mathbf{T}}^{inter}$, and eq. (8) imposes that the applied laser power values should be above a lower bound $\underline{\mathbf{P}}$.

In both cases, the laser power $\mathbf{P}_\ell$ on each grouped layer ℓ is defined as the control vector. Noting that both the output $\mathbf{T}_\ell^{inter}$ and input $\mathbf{P}_\ell$ are vectors with a dimension of $m_\ell \times 1$, the control problem is a $m_\ell \times m_\ell$ multi-input, multi-output (MIMO) control problem. Depending on the grouped layer number ℓ, the m_ℓ nodes on a grouped layer ℓ may consist of part nodes and

support nodes. Hence, the control formulations here allow optimizing laser powers for melting both the part components and support structures. For simplicity, the subsequent simulation and experimental validation only consider controlling the laser powers for melting the part components (inner- and outer-walls) while leaving the laser power for melting the support structures at their default value given by the manufacture.

OPT1 is a convex program and it is solved by using the MATLAB package *cvx*, which applies a primal-dual interior-point algorithm through the SEDUMI/SDPT3 solvers. It takes 35 s to solve OPT1 for the entire build of 70 grouped layers on a Dell laptop with Intel® Core i7-3632QM CPU, 2.20 GHz. For OPT2, depending on the lower bound $\underline{\mathbf{P}}$ in eq. (8), there may not exist a feasible solution to satisfy the interlayer temperature constraint defined in eq. (7). If the optimal laser power turns out to be less than the lower bound in solving eq. (6) - eq. (7), it is set to the lower bound. In this study, a lower bound of 228 W is imposed on laser power in OPT2. This is a 20% reduction from its default value of 285 W and considered to be a safe estimate without causing lack of fusion under the room temperature [15, 33]. Table 1 lists the other process parameters used in the simulations and the experimental validation.

Fig. 3 shows the optimization results for OPT1 and OPT2, where the target threshold for interlayer temperature is set to be 200 ^oC. Fig. 3(a) (right vertical-axis) shows the optimal laser power profile obtained from OPT1, and Fig. 3(a) (left vertical-axis) shows the resulting interlayer temperatures. Both the inner- and outer-wall interlayer temperatures are maintained under the target threshold during the entire simulated build process. For the first 35 grouped layers where both the inner- and outer-wall interlayer temperatures are below the threshold value of 200 ^oC, the default laser power of 285 W is used for both walls. After the grouped layer 35, the laser power for the inner-wall has to be reduced to ensure that the inner-wall interlayer temperatures stay below the target threshold. After the grouped layer 50, the laser power for the inner-wall starts to increase

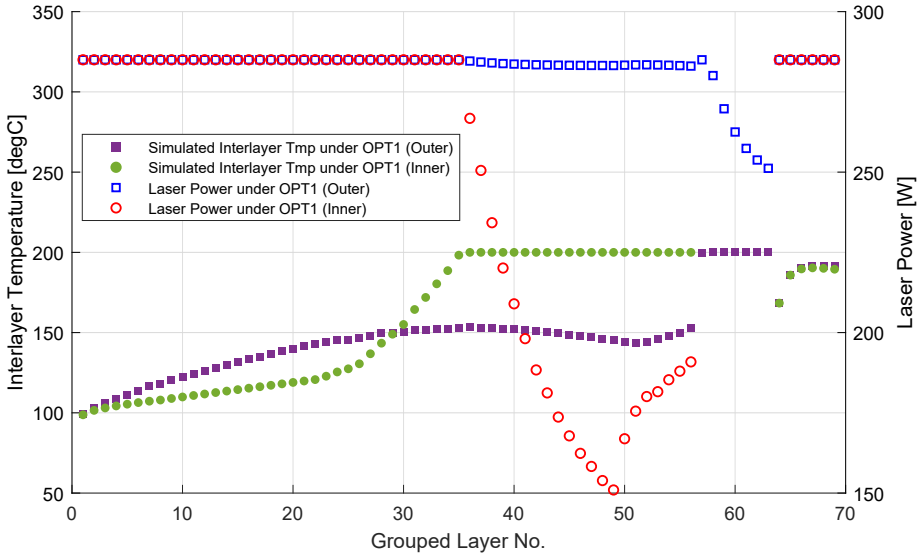

(a) OPT1

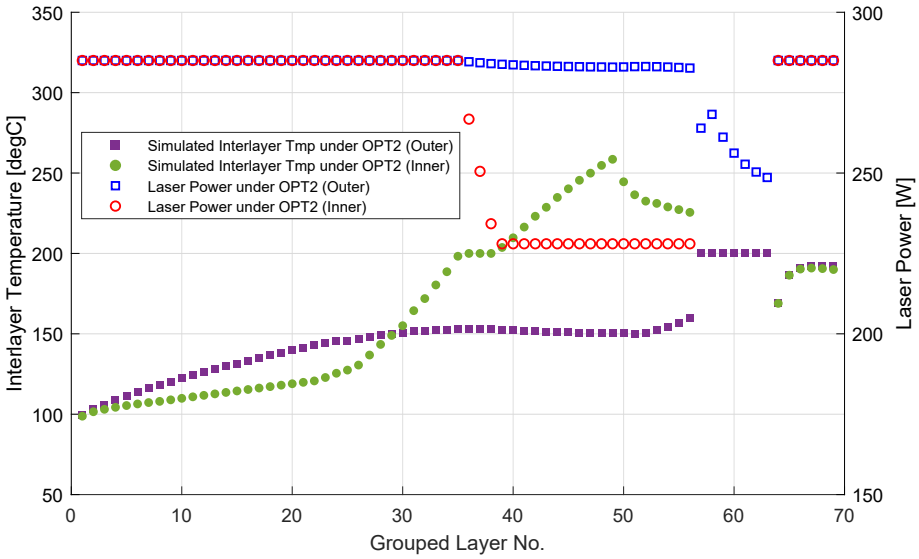

(b) OPT2

Figure 3: Optimal control of interlayer temperature for the square-canonical geometry: controlled interlayer temperatures (left y-axis) and optimal laser power inputs (right y-axis); inner-wall and outer-wall merge at grouped layers 57 - 63 and thus only outer-wall temperatures are shown. (a) OPT1; (b) OPT2.

Table 1: Process parameters used in simulations and experimental validation.

Parameter	Value	Unit
Recoating time between two physical layers	8.5	s
Laser spot size	80 [34]	μm
Default laser power (part)	285	W
Default laser power (support structure)	100	W
Laser transmission efficiency	0.4	-
Laser scan speed (part)	960	mm/s
Laser scan speed (support structure)	900	mm/s
Ambient temperature T_a	25	^oC
Substrate preheating temperature	80	^oC
Hatch space	0.11	mm
Thickness of a physical layer	0.04	mm
Thickness of a grouped layer of 18 physical layers	0.72	mm
Substrate thickness	30	mm
Solid volume fraction of support	0.27	-

from its lowest value of 150 W. The laser power for the outer wall stays close to 285 W before the outer-wall merges with the inner-wall at the grouped layer 57, after which the laser power for the junction is reduced to ensure its interlayer temperatures stay below the threshold value of 200 ^oC. When the two walls separate again at the grouped layer 64, the predicted interlayer temperatures for both walls are below the threshold value and thus the default laser power of 285 W is applied for both walls.

For OPT2, Fig. 3(b) shows that up to the grouped layer 38, the optimal laser power profile (right vertical-axis) overlaps with its counterpart under OPT1. From the grouped layer 39 to layer 56, there is no feasible solution that simultaneously satisfies both constraints on the inner-wall interlayer temperature and on the inner-wall laser power. As a result, when the inner-wall laser power is saturated at its lower bound of 228 W, the corresponding inner-wall temperatures have exceed the target threshold, with a maximum overshoot of 58.6 ^oC beyond the threshold. For the

grouped layers higher than 56, the interlayer temperatures follow a similar trend as in OPT1.

2.4 Experimental setup

2.4.1 Implementation of optimized laser power profiles

The optimal laser power inputs of OPT1 and OPT2 shown in Fig. 3 (right y-axis) are then implemented on the EOS M280 L-PBF system. A flow chart is given in Fig. 4. First, STLs for the inner-wall slice and outer-wall slice of each grouped layer are generated. These STLs, together with their respective laser power values, are then used by the machine operator to program each optimization scheme as a feed-forward control.

2.4.2 Optimization cases

For each optimization scheme (OPT1 and OPT2), multiple samples are built, as summarized in Table 2. Full-build samples with 1270 physical layers are fabricated to validate the proposed thermal control. In addition, partial-build samples are fabricated and post-processed (see Sec. 2.4.4) to investigate the effect of control on the melt-pool size and microhardness. The samples built with the default laser power of 285 W from our prior studies [3,22] are included in Table 2 as the baseline (BL-) samples for comparison. BL-300 and BL-876 are samples for which the build process stops after finishing the physical layer no. 300 and no. 876, respectively. They are built to compare the melt-pool cross-sections of the outer-wall at layer 300 (with interlayer temperature at about 100 ^oC) and the melt-pool cross-sections of the inner-wall at layer 876 (with interlayer temperature at about 300 ^oC) [22]. Stopping the build process at a specific layer ensures that the melt-pool cross-sections at that layer will not be covered by subsequent layers and thus can be fully characterized. The physical layers 300 and 876 are strategically chosen so that the melt-pool cross-sections from the two layers having the largest difference in interlayer temperatures can be directly compared [22].

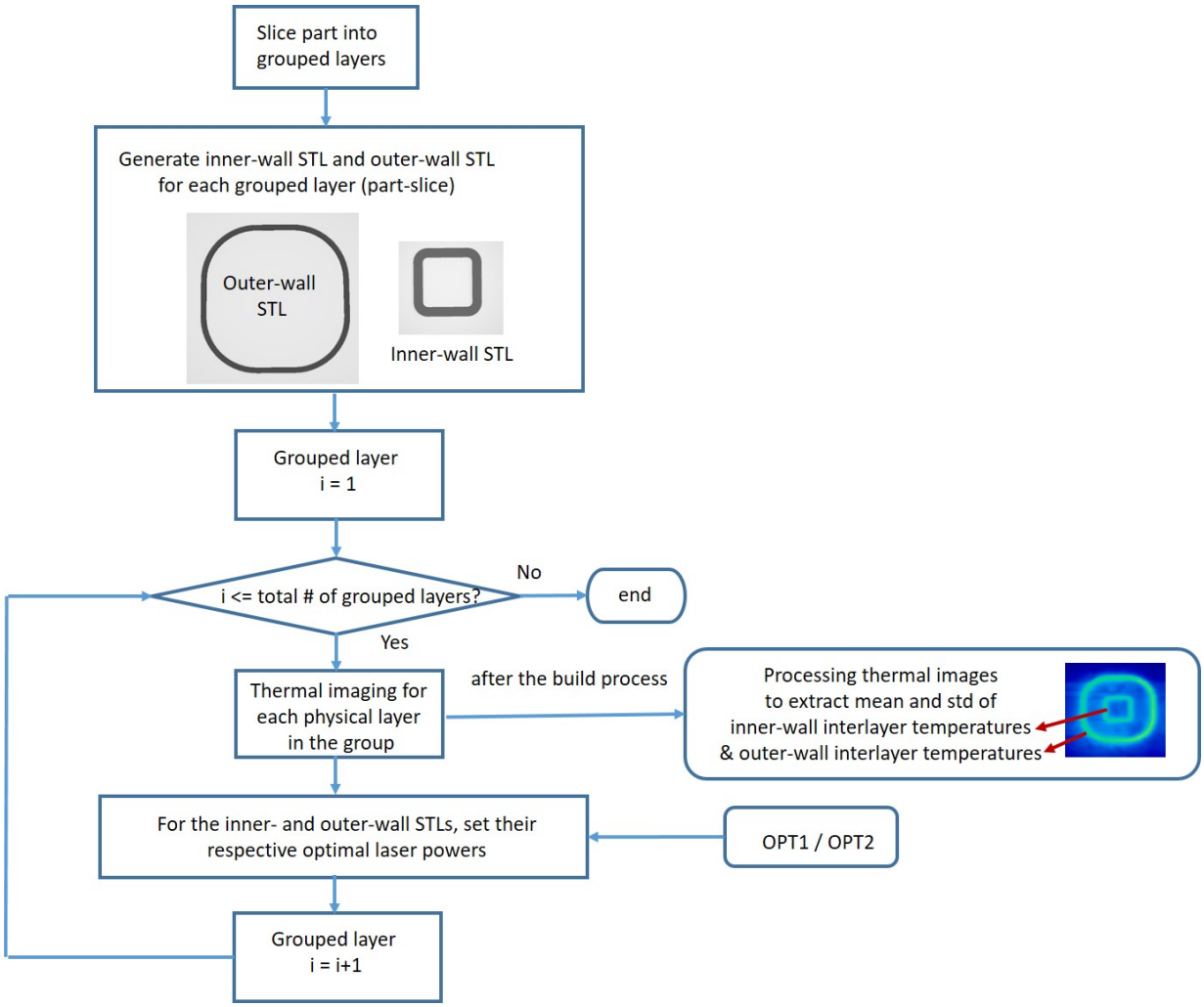

Figure 4: Flow chart of implementing the optimal laser power profile as a feed-forward control.

Table 2: Samples built with different laser-power strategies and different number of layers.

Samples (Purpose)	Full build of 1270 layers (Interlayer temp validation)	Partial build of 300 layers (Micrograph and microhardness on outer-wall sections)	Partial build of 876 layers (Micrograph and microhardness on inner-wall sections)
BASELINE [3, 22]	BL-FullBuild	BL-300	BL-876
OPT1	OPT1-FullBuild	-	OPT1-876
OPT2	OPT2-FullBuild	-	OPT2-876

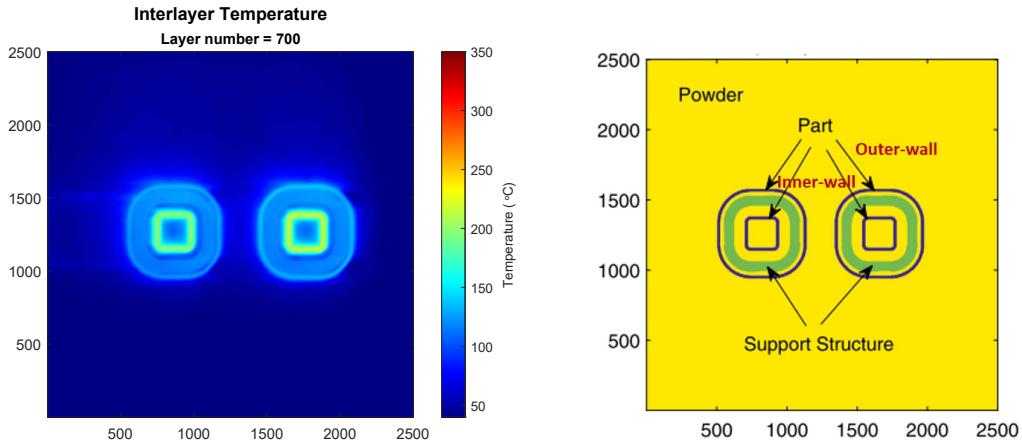

(a) (b)

Figure 5: (a) Interlayer temperature distribution at physical layer 700 under OPT2; (b) Sample layer mask derived from STL to identify the inner- and outer-wall regions from each thermal image.

As indicated by Fig. 3, the laser power melting the physical layer 300 (in grouped layer 17) remains at the default level of 285 W, under either OPT1 or OPT2. Consequently, partial builds of 300 layers are not repeated for OPT1 and OPT2. Only partial builds of 876 layers are repeated under OPT1 and OPT2 (OPT1-876 and OPT2-876) to be compared with the baseline samples.

2.4.3 In-situ layer-wise thermal imaging

For OPT1-FullBuild and OPT2-FullBuild, in-situ thermographic imaging developed in our prior work [3] is used to capture the temperature history of the top surface during each build process.

Specifically, an IR camera FLIR X6801sc is mounted on top of the EOS chamber to monitor and capture images of the entire powder bed area through the chamber top viewport. Then, the thermal image of interlayer temperature distribution before melting each new layer is extracted at the exact moment when the recoater finishes the powder spreading. That is, the thermal data is collected at step 3 of each laser processing cycle: 1) laser melts a physical layer; 2) recoater spreads a layer of powder; 3) register the image of interalyer temperature; and 4) laser starts to scan the next physical layer.

The thermographic radiance data recorded by the IR camera are converted into temperature outputs in Celsius (^oC) through a lookup table obtained from an offline calibration process in [3] (see also Appendix B). Fig. 5(a) shows the interlayer temperature distribution in Celsius for the entire physical layer 700 under OPT2, including the left/right canonical parts and the power bed. Fig. 5(b) shows a sample mask derived from the STL slice. The mask is used to identify a region of interest (e.g., inner- or outer-wall) from the temperature image of a physical layer so that the mean and standard deviation of the temperature distribution in that region can be computed. The resulting inner- and outer-wall interlayer temperatures in each layer are then used to validate the part-level thermal control given in Sec. 2.3.

2.4.4 Micrograph and microhardness measurements

In order to make a direct comparison with the baseline samples (BL-300 and BL-876) built in [22], this study follows the same procedure for part sectioning and micrograph. Fig. 6(a) illustrates the two sectioning cuts (Cut 1 and Cut 2) in the XZ plane performed on each partial-build sample. Considering the hatch length of 15 mm (see Fig. 2), Cut 1 is made to study the melt-pool cross-sections close to the end-of-hatch, reflecting how the change of laser scanning direction affects the melt-pool cross-sectional area; and Cut 2 is made to study the melt-pool cross-sections at the

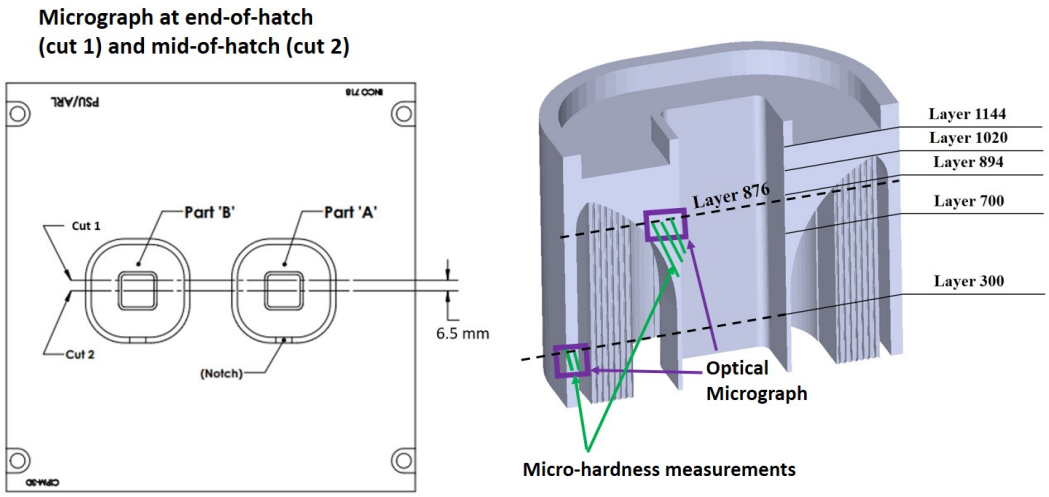

(a) (b)

Figure 6: Illustration of (a) part sectioning and (b) areas for micrograph and hardness measurements.

mid-of-hatch, reflecting the melt-pool's steady-state size.

For each sectioning, micrographs are performed for the outer wall of BL-300 and inner walls of BL-876, OPT1-876, and OPT2-876. Fig. 6(b) provides a schematic illustration on where the micrograph is taken on the left-quarter of the geometry (same locations on the right-quarter not shown for simplicity). The corresponding samples are then polished and etched, and a Keyence VHX-7100 optical microscope is used to capture the metallographic images. As illustrated in Fig. 6(b), microhardness testings are performed for the same areas as the micrographs to assess the local mechanical properties, using the Qness Q60 A+ microindenter through its Vickers indenter, with a test force of 0.1 kg of force (kgf).

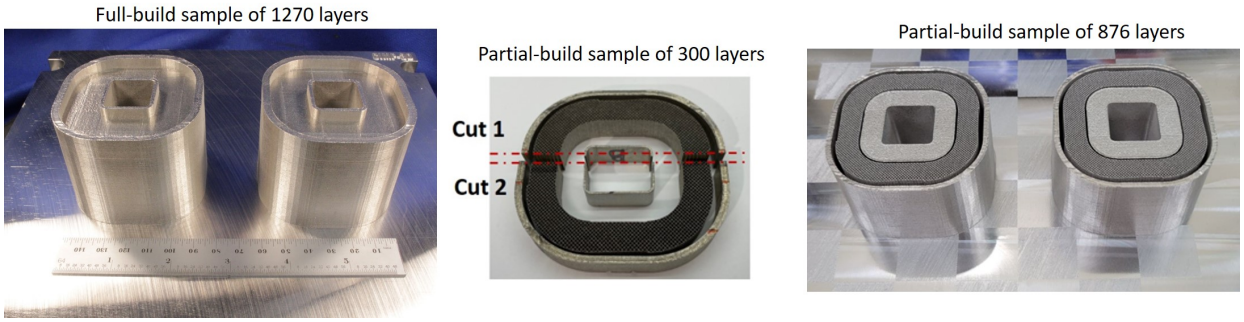

Figure 7: Images of sample builds.

3 Experimental Results and Discussions

3.1 Interlayer temperatures

Fig. 7 shows images of multiple samples with different number of physical layers. For full-build samples, Fig. 8 plots the mean trajectory and standard deviation of the in-situ measurements of the inner- and outer-wall interlayer temperatures with respect to the *physical* layer numbers under each laser-power strategy. All measurements correspond to the right canonical part (see Fig. 5(a) for a sample thermal image of the left/right canonical parts). It is shown that except physical layers 1000 - 1144, OPT1 is able to meet the target threshold for interlayer temperatures. OPT2, albeit not able to meet the target, has reduced the interlayer temperatures during physical layers 648 - 1000 compared to the BL-FullBuild.

Recall that the inner- or outer-wall of each grouped layer is represented by a node in the FD model in Sec. 2.2. As a result, the model-based optimization in Sec. 2.3 directly controls the *mean* of the inner- or outer-wall interlayer temperature in each *grouped* layer. To validate such control objective, Fig. 9 only plots the mean trajectories of the inner- and outer-wall interlayer temperatures to compare different laser power schemes, where the standard deviations are not shown for clarity of the illustration. The readers are referred to Fig. 15 in Appendix B for the

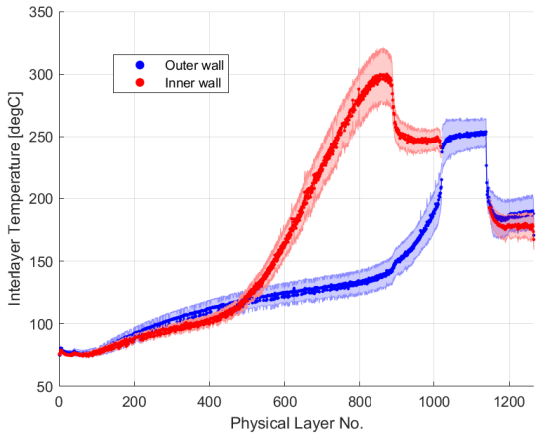

(a) BL-FullBuild

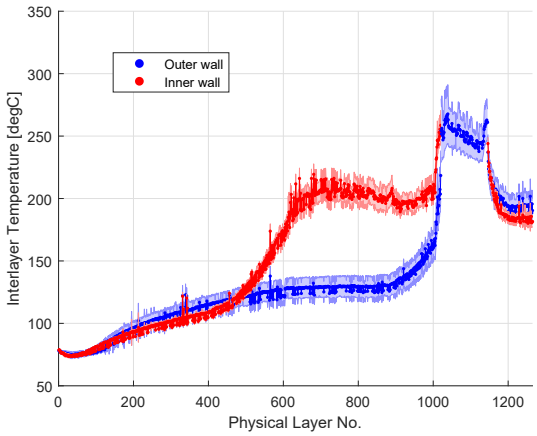

(b) OPT1-FullBuild

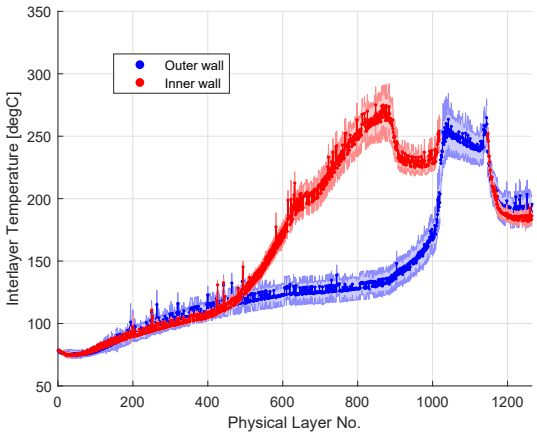

(c) OPT2-FullBuild

Figure 8: Mean trajectories and standard deviations of inner- and outer-wall interlayer temperature measurements with respect to the physical layer numbers, under each laser-power strategy (BL, OPT1 and OPT2).

standard deviations.

Fig. 9 shows that for the grouped layers before 36 or later than 64, the controlled mean inner-wall or mean outer-wall interlayer temperatures (under either OPT1 or OPT2) resemble their respective uncontrolled counterparts, as the optimized laser powers end up staying at the default value of 285 W for these layers (see Fig. 3). Under OPT1, the mean inner-wall interlayer temperatures during the grouped layers 37 - 55 are closely aligned with the anticipated threshold, indicating that the control objective is met. Under OPT2, the mean inner-wall interlayer temperatures during the grouped layers 37 - 39 are aligned with the threshold value. However, as the laser power for the inner-wall is saturated at its lower bound in the grouped layers 40 - 56 (see Fig. 3(b)), the corresponding controlled inner-wall interlayer temperatures have exceeded the target threshold. Nevertheless, compared to BL, OPT2 has reduced the inner-wall interlayer temperatures by up to 40 ^oC (or 13%) in the grouped layers 40 - 56.

Remark: Under OPT1, during the physical layers 1000 - 1144 (grouped layers 56 -63) where the two walls grow closer and then merge into one junction, the temperatures are close to 250 ^oC and thus do not meet the target threshold. Note that the optimal laser powers are dropped for scanning the junction layers (see Fig. 3(a) for simulation results), but the reductions are not large enough to lower the temperatures sufficiently. One potential source for not meeting the target temperature threshold is due to modeling errors where the junction interlayer temperatures are under-estimated, possibly attributed to the simplification of the powder elements used in the FD modeling [19]. Another reason for not meeting the temperature threshold is possibly attributed to the way of programming the optimal laser power for each STL slice in EOS M280 (see Fig. 4). In the experiment, the default downskin and upskin of the machine setup are turned off to prevent the EOS toolpath software from interpreting the bottom of each part slice as a downskin. As a result, the default machine downskin-power of 95 W and upskin-power of 153 W are overridden by the

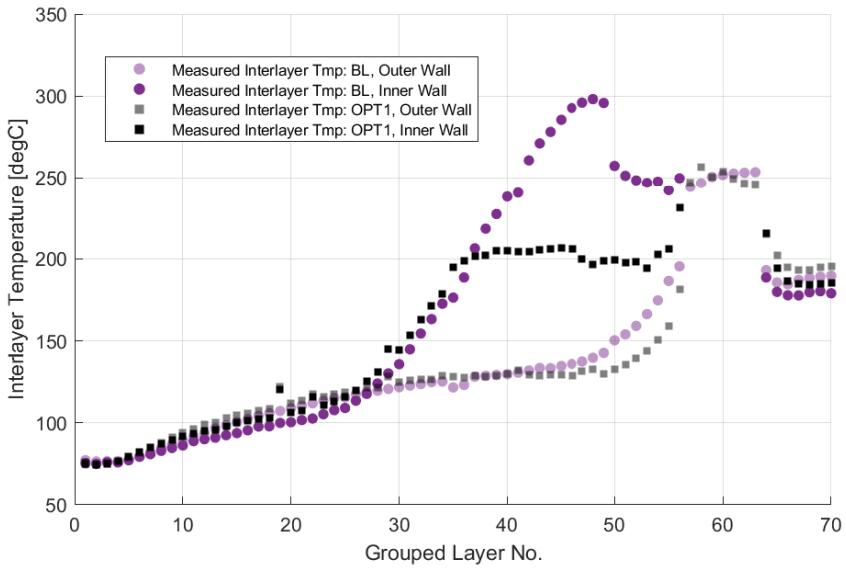

(a) OPT1-FullBuild vs BL-FullBuild

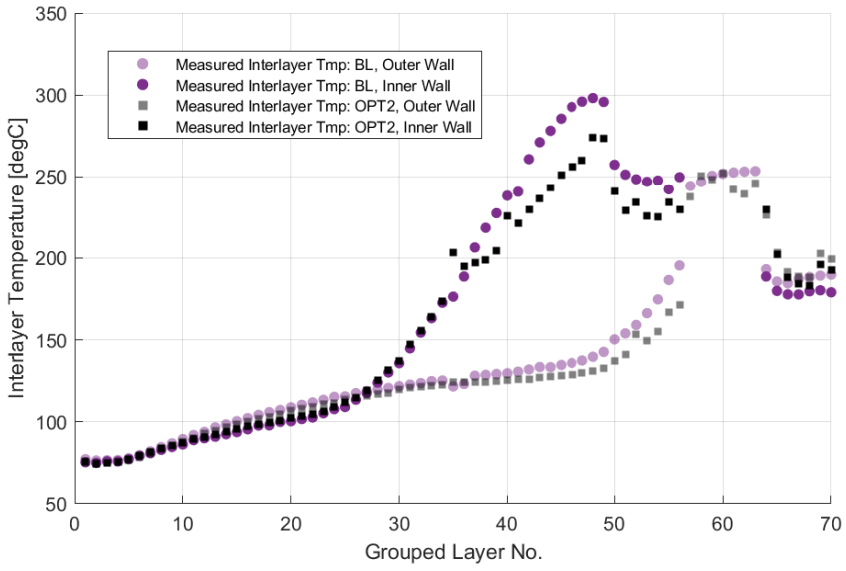

(b) OPT2-FullBuild vs BL-FullBuild

Figure 9: Mean of measured interlayer temperatures w.r.t the grouped layer numbers, under (a) OPT1 versus BL and (b) OPT2 versus BL. Standard deviation not shown for clarity.

higher power values from OPT1. Such machine programming modification has the most impact on processing the junction as it has the largest downskin and upskin areas.

3.2 Melt-pool dimensions

As stated in Table 2, micrographs are performed on the outer-wall of BL-300 and inner-walls of BL-876, OPT1-876 and OPT2-876. For all partial-build samples, only the melt-pool dimensions from the *top layer* of each sample are measured and included for comparison, as discussed in Sec. 2.4.4. Fig. 10 shows the optical micrographs of the melt-pool cross-sections from the inner wall of sample OPT1-876. Lack-of-fusion defects are clearly visible and gaps exist between some neighboring melt-pools on the top layer. Such lack-of-fusion defects are not totally unexpected considering that the laser power for the inner-wall has dropped to as low as 150 W at the physical layer 876 (in grouped layer 49), as shown in Fig. 3(a). This indicates that although the optimal laser-power strategy OPT1 has achieved the objective of ensuring the interlayer temperatures below the target threshold (except the junction), it has caused severe defects and thus is excluded from further comparisons. Statistics of the melt-pool dimensions from OPT1-876 are given in Appendix C for completeness.

Fig. 11 compares the micrographs of the mid-of-hatch melt-pool cross-sections among BL-300, BL-876, and OPT2-876. The sample melt-pool micrograph for OPT2-876 is taken from a different surface side from those of BL-300 and BL-876, which explains why it shows the opposite hatch sequence from the BL micrographs. Fig. 12 compares the micrographs for the end-of-hatch melt-pool cross-sections. The melt-pool dimensions (mean and std) from the top layer of each partial-build sample are given in Table 3 (for mid-of-hatch cross-sections) and Table 4 (for end-of-hatch cross-sections) to reflect how melt-pool dimensions are affected by the interlayer temperature and laser power resulted from different laser-power strategies. In addition, using the melt-pool dimensions from the top layer of sample BL-300 as a baseline, the percentage of change in melt-

(a) Mid-of-hatch, inner-wall

(b) End-of-hatch, inner-wall

Figure 10: OPT1-876: micrographs of inner-wall cross-sections show lack-of-fusion defects.

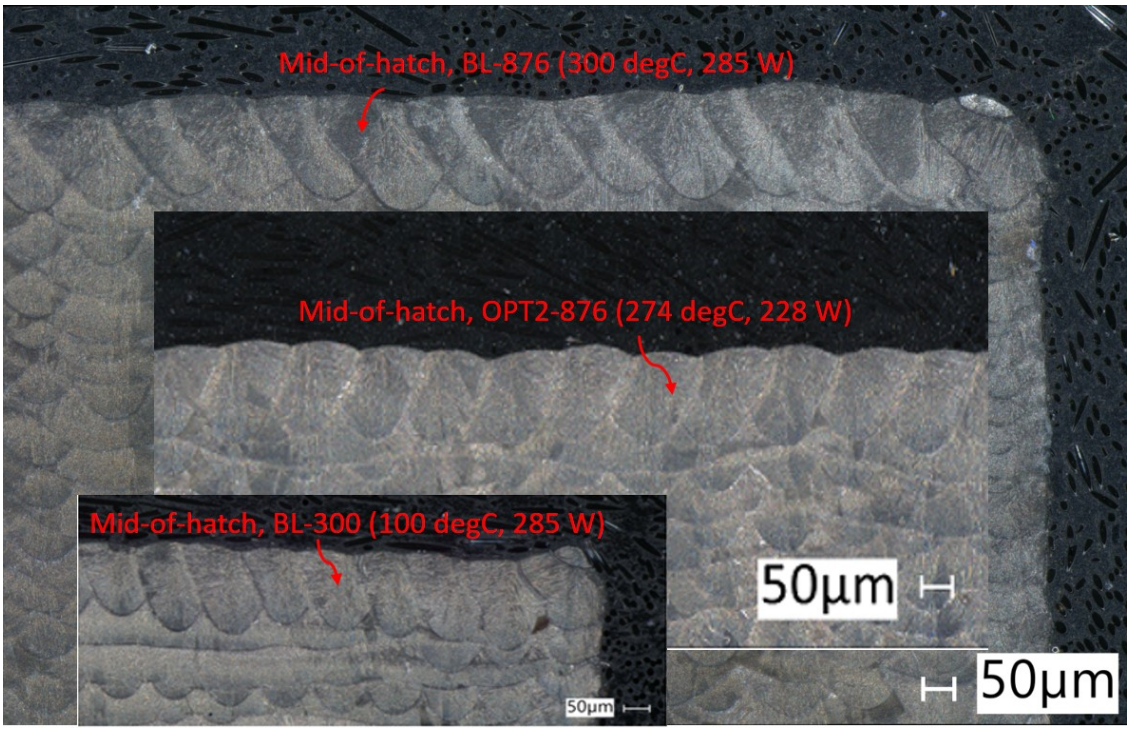

Figure 11: Comparison of the mid-of-hatch melt-pool cross-sections at the top layer of OPT2-876 (274 ^oC, 228 W) to melt-pools of BL-300 (100 ^oC, 285 W) and BL-876 (300 ^oC, 285 W) from [22].

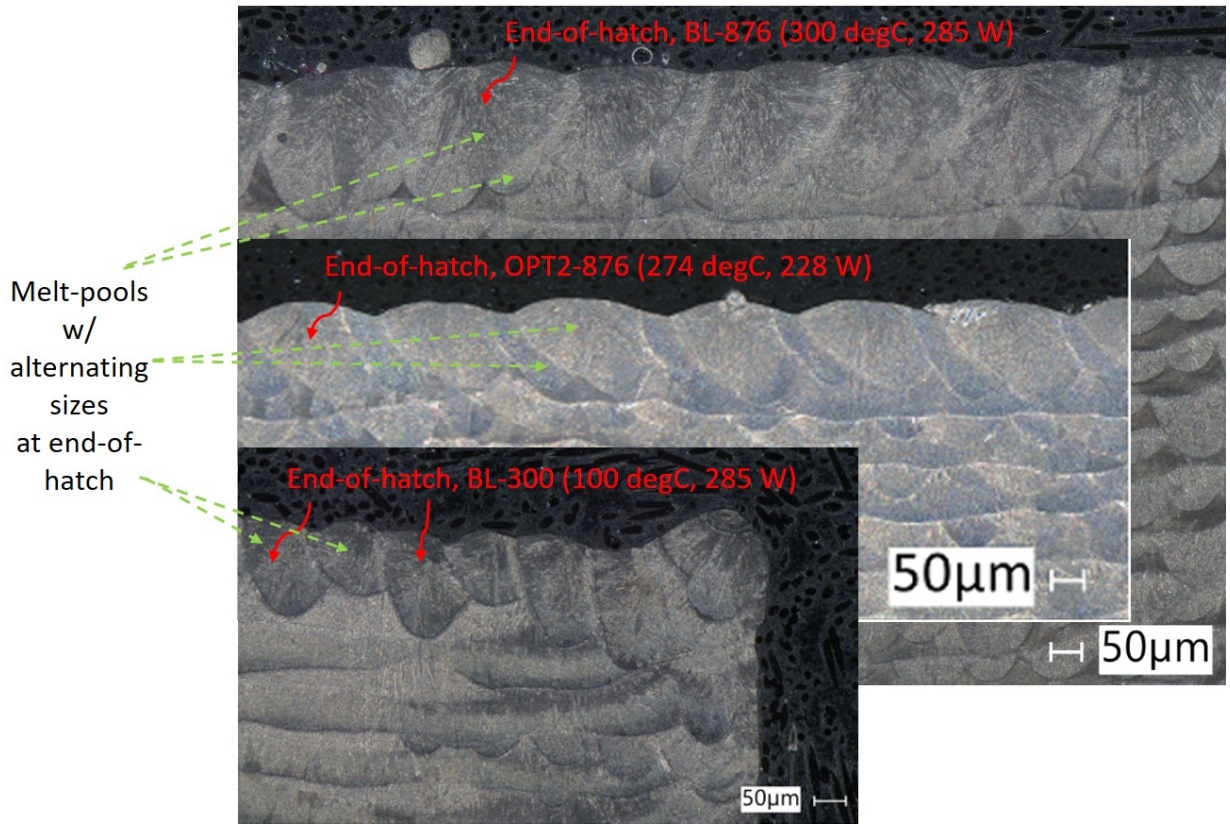

Figure 12: Comparison of the end-of-hatch melt-pool cross-sections at the top layer of OPT2-876 (274 ^oC, 228 W) to melt-pools of BL-300 (100 ^oC, 285 W) and BL-876 (300 ^oC, 285 W) from [22].

Table 3: Mid-of-hatch cross-sections: melt-pool dimensions (mean ± std) and percentage of change with respect to BL-300. p-value is calculated using unequal variance t-test; For $p > 0.05$, % of change is deemed not statistically significant.

Build	Physical layer No. (interlayer temp, power)	Half-width		Depth	
		value (μm)	% of change (p-val)	value (μm)	% of change (p-val)
BL-300 [22]	300 (100 ^oC, 285 W)	89.6±5.5	0%	173.9±13.4	0%
BL-876 [22]	876 (300 ^oC, 285 W)	125.7±11.7	↑ 40.3 % ($p < 0.001$)	167.1±12.0	↓ 3.9% ($p = 0.2$)
OPT2-876	876 (274 ^oC, 228 W)	93.9±8.3	↑ 4.8 % ($p = 0.04$)	142.2±9.8	↓ 18.2% ($p < 0.001$)

Table 4: End-of-hatch cross-sections: melt-pool dimensions (mean ± std) and percentage of change with respect to BL-300. Only the post-laser-turn melt pools are included. For $p > 0.05$, % of change is deemed not statistically significant.

Build	Physical layer No. (interlayer temp, power)	Half-width		Depth	
		value (μm)	% of change (p-val)	value (μm)	% of change (p-val)
BL-300 [22]	300 (100 ^oC, 285 W)	76.4±7.2	0%	161.8±14.8	0%
BL-876 [22]	876 (300 ^oC, 285 W)	179.3±14.6	↑ 134.7% ($p < 0.001$)	220.2±27.4	↑ 36.1% ($p < 0.001$)
OPT2-876	876 (274 ^oC, 228 W)	138.7±15.9	↑ 81.5% ($p < 0.001$)	138.8±14.4	↓ 14.2% ($p < 0.002$)

pool dimensions for each sample is given. Readers are referred to Appendix C regarding how the melt-pool half-width and depth are measured from the micrographs.

Mid-of-hatch Consider the top layer of each sample shown in Fig. 11. They are processed with different laser powers, where the top layer of OPT2-876 (in grouped layer 49) is scanned with 228 W and the BL samples are scanned with 285 W. The mean interlayer temperature for the top layer of each sample is extracted from Fig. 8. Both factors (temperature and laser power) affect the melt-pool dimensions. It is shown that for each sample, the top layer has pretty uniformly sized

melt-pools. Under the default laser power of 285 W, the melt-pool mean half-width of BL-876 is 40% larger than its counterpart from BL-300, attributed to the 200 ^oC increase in the interlayer temperature. Compared to BL-876, the average top-layer melt-pool size of OPT2-876 is visibly reduced, attributed to both the reduced laser power (dropped from 285 W to 228 W) and the reduced interlayer temperature (dropped from 300 ^oC to 274 ^oC). Table 3 shows that the mean half-width of OPT2-876 is only slightly larger (about 5% larger) than its counterpart from BL-300, in contrast to the melt-pool half-width of BL-876 being 40% larger than BL-300. Overall, OPT2 has reduced the melt-pool mean half-width at layer 876 by about 25% compared to the uncontrolled case (BL-876). This indicates that OPT2 has reduced the variability of melt-pool half-width along the build direction compared to the uncontrolled case BL.

The sample variation in melt-pool mean depth between BL-300 and BL-876 is not statistically significant, but OPT2-876 has a reduced melt-pool mean depth compared to the other two samples.

End-of-hatch Fig. 12 shows that for each sample, the end-of-hatch melt-pool cross-sections in the top layer exhibit alternating sizes, where the post-laser-turn melt-pools are larger than their respective pre-laser-turn melt-pools. By comparing only the post-laser-turn melt-pool cross-sections among the three samples, we see a similar trend as observed for the mid-of-hatch melt-pool cross-sections, but with a much amplified difference in magnitude reflecting the effect of local temperature increase due to the laser turnaround from hatch to hatch. Table 4 shows that for the uncontrolled case, the end-of-hatch melt-pool mean half-width in the top layer of BL-876 is about 130% larger than its counterpart of BL-300. Under OPT2, the melt-pool mean half-width in the top layer of OPT2-876 has reduced by more than 20% compared to the uncontrolled BL-876. The end-of-hatch melt-pool mean depth in the top layer of OPT2-876 has reduced by more than 36% compared to BL-876 and by more than 14% compared to BL-300.

Table 5: Microhardness comparison among three samples at the examined area.

	BL-300	BL-876	OPT2-876
% of test points having microhardness $\geq$ 297 HV	100%	86.1%	91.6%
% of test points having microhardness $\geq$ 318 HV	69.3%	36.0%	47.8%

3.3 Microhardness

Microhardness is considered as an indicator on how a material is able to deform plastically and it is correlated with the material's yield strength [35]. Fig. 13 shows comparison of the Vickers microhardness maps taken from the outer-wall of BL-300 and from the upper inner-walls of BL-876 and OPT2-876 (see areas of measurements illustrated in Fig. 6(b)). Table 5 compares the percentage of test points in the examined area of each sample having microhardness above a specific level, namely 297 HV or 318 HV. The baseline sample BL-300 has 100% of its test points above 297 HV and 69.3% of test points above 318 HV. For the uncontrolled case, the upper inner-wall of BL-876 has a reduced percentage of test points above each specified microhardness level (297 HV or 318 HV) compared to BL-300, indicating a reduced hardness along the build direction. Compared to BL-876, the upper inner-wall of OPT2-876 has 6% increase in the percentage of test points above 297 HV and 32% increase in the percentage of test points above 318 HV, indicating improved microhardness under OPT2.

The hardness variation across the three samples could be attributed to the change of cooling rates described as follows. An approximate calculation of the average cooling rate at the center line of a weld is given in Kistler et al. [36],

$$\frac{dT}{dt} = 2\pi k \frac{v}{\eta Q}(T_m - T_0)^2 \tag{9}$$

where k is the thermal conductivity, v is the processing speed, η is the laser efficiency, Q is the laser power, T_m is the melting temperature, and T_0 is the substrate predeposition temperature.

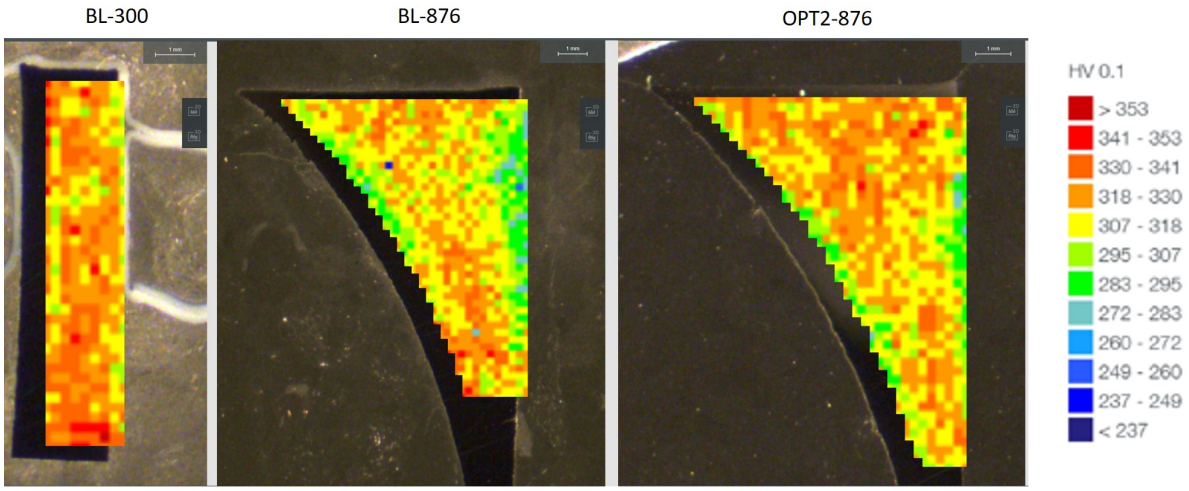

Figure 13: Comparison of microhardness maps among BL-300, BL-876, and OPT2-876.

Eq. (9) is used here for qualitative analysis. It indicates that under the same laser power of 285 W, the increase in interlayer temperatures (can be viewed as the predeposition temperature T_0 here) from lower values for BL-300 to higher values for the upper inner-wall of BL-876 will render slower cooling rates for BL-876, contributing to reduced hardness for BL-876. By comparing OPT2-876 and BL-876, the reduced laser power Q used in OPT2-876 will increase the cooling rate, and the reduced interlayer temperatures in OPT2-876 will further increase the cooling rate. Hence, OPT2-876 is expected to have higher cooling rates than BL-876 and thus helps recover its hardness.

4 Conclusion

This paper presents a part-level optimization of laser power as a feed-forward control of interlayer temperature for L-PBF processes. The optimization of (FD) node-dependent laser powers enables the control of each geometric feature in a grouped layer with an individualized laser power. Two specific optimal control schemes are investigated, with or without a lower bound on laser power, and they are experimentally validated using a square-canonical geometry. Experimental results show that the optimal laser-power scheme without a lower bound (OPT1) is capable of reducing

the interlayer temperatures below the target threshold except at the junction of the inner- and outer-walls due to modeling errors and implementation limitations with the EOS M280 system. However, the significantly reduced laser power (up to 50%) from its default value in OPT1 has resulted in lack-of-fusion defects. By imposing a lower bound on laser power, the resulting optimal laser-power scheme OPT2 has effectively reduced the interlayer temperatures albeit not meeting the target threshold due to control saturation at its lower bound. Experimental results also show that OPT2 has reduced the variability of the melt-pool size along the build direction. Overall, the melt-pool mean half-width at layer 876 under OPT2 has reduced by more than 20% compared to the uncontrolled BL-876. In addition, for microhardness measurements in the area of interest close to layer 876, OPT2 has 6% increase in the percentage-of-test-points above 297 HV and 32% increase in the percentage-of-test-points above 318 HV compared to the uncontrolled case, indicating improved hardness under OPT2.

This paper has only used laser power as a knob for controlling interlayer temperatures. Experimental results indicate that to avoid lack of fusion, the design space of laser power is limited. Interlayer dwell time was used as an additional knob in [15] to further reduce overheating. However, applying a common dwell time for the entire part layer as in [15] might not work well for a complex geometry where a layer consists of both hot and cold regions. The added interlayer dwell time will help reduce the temperature of the hot region but will further cool down the cold region, which would increase the risk of creating shrink lines in the build.

Acknowledgment This work was supported in part by the U.S. National Science Foundation under Grant No. 2015930. The authors would like to thank Mr. Scott Tokarz at the Applied Research Lab (ARL) of Penn State for his work on performing the micrographs and microhardness measurements of the experimental samples.

References

[1] Cooke, S., Ahmadi, K., Willerth, S., and Herring, R., 2020. "Metal additive manufacturing: Technology, metallurgy and modelling". *Journal of Manufacturing Processes,* ***57***, pp. 978–1003.

[2] Calignano, F., 2014. "Design optimization of supports for overhanging structures in aluminum and titanium alloys by selective laser melting". *Materials & Design,* ***64***, pp. 203–213.

[3] Wang, Q., Michaleris, P., Pantano, M., Li, C., Ren, Y., and Nassar, A. R., 2022. "Part-scale thermal evolution and post-process distortion of inconel-718 builds fabricated by laser powder bed fusion". *Journal of Manufacturing Processes,* ***81***, pp. 865–880.

[4] Grasso, M., Laguzza, V., Semeraro, Q., and Colosimo, B. M., 2017. "In-process monitoring of selective laser melting: spatial detection of defects via image data analysis". *Journal of Manufacturing Science and Engineering,* ***139***(5), p. 051001.

[5] Sames, W. J., List, F., Pannala, S., Dehoff, R. R., and Babu, S. S., 2016. "The metallurgy and processing science of metal additive manufacturing". *International materials reviews,* ***61***(5), pp. 315–360.

[6] Yeung, H., Lane, B., and Fox, J., 2019. "Part geometry and conduction-based laser power control for powder bed fusion additive manufacturing". *Additive Manufacturing,* ***30***, p. 100844.

[7] Martin, A. A., Calta, N. P., Khairallah, S. A., Wang, J., Depond, P. J., Fong, A. Y., Thampy, V., Guss, G. M., Kiss, A. M., Stone, K. H., et al., 2019. "Dynamics of pore formation during laser powder bed fusion additive manufacturing". *Nature communications,* ***10***(1), p. 1987.

[8] Wang, Q., Michaleris, P. P., Nassar, A. R., Irwin, J. E., Ren, Y., and Stutzman, C. B., 2020. "Model-based feedforward control of laser powder bed fusion additive manufacturing". *Additive Manufacturing,* ***31***, p. 100985.

[9] Vasileska, E., Demir, A. G., Colosimo, B. M., and Previtali, B., 2020. "Layer-wise control of selective laser melting by means of inline melt pool area measurements". *Journal of Laser Applications,* ***32***(2).

[10] Craeghs, T., Bechmann, F., Berumen, S., and Kruth, J.-P., 2010. "Feedback control of layer-wise laser melting using optical sensors". *Physics Procedia,* ***5***, pp. 505–514.

[11] Wang, R., Standfield, B., Dou, C., Law, A. C., and Kong, Z. J., 2023. "Real-time process monitoring and closed-loop control on laser power via a customized laser powder bed fusion platform". *Additive Manufacturing,* ***66***, p. 103449.

[12] Gunasegaram, D., Barnard, A., Matthews, M., Jared, B., Andreaco, A., Bartsch, K., and Murphy, A., 2024. "Machine learning-assisted in-situ adaptive strategies for the control of defects and anomalies in metal additive manufacturing". *Additive Manufacturing*, p. 104013.

[13] Ma, C., Wang, D., Zhao, K., Gao, J., Wang, H., Zhang, A., Cheng, L., and Zhang, Y., 2024. "Layer-wise surface quality improvement in laser powder bed fusion through surface anomaly detection and control". *Computers & Industrial Engineering,* ***191***, p. 110098.

[14] Vasileska, E., Demir, A. G., Colosimo, B. M., and Previtali, B., 2022. "A novel paradigm for feedback control in lpbf: layer-wise correction for overhang structures". *Advances in Manufacturing,* ***10***(2), pp. 326–344.

[15] Riensche, A., Bevans, B. D., Smoqi, Z., Yavari, R., Krishnan, A., Gilligan, J., Piercy, N., Cole, K., and Rao, P., 2022. "Feedforward control of thermal history in laser powder bed fusion:

Toward physics-based optimization of processing parameters". *Materials & Design,* ***224***, p. 111351.

[16] Kavas, B., Balta, E. C., Tucker, M., Rupenyan, A., Lygeros, J., and Bambach, M., 2023. "Layer-to-layer closed-loop feedback control application for inter-layer temperature stabilization in laser powder bed fusion". *Additive Manufacturing,* ***78***, p. 103847.

[17] Li, C., Gouge, M. F., Denlinger, E. R., Irwin, J. E., and Michaleris, P., 2019. "Estimation of part-to-powder heat losses as surface convection in laser powder bed fusion". *Additive Manufacturing,* ***26***, pp. 258–269.

[18] Gouge, M., Denlinger, E., Irwin, J., Li, C., and Michaleris, P., 2019. "Experimental validation of thermo-mechanical part-scale modeling for laser powder bed fusion processes". *Additive Manufacturing*.

[19] Ren, Y., and Wang, Q., 2023. "A finite difference method for fast prediction and control of part-scale temperature evolution in laser powder bed fusion". *Journal of Manufacturing Processes,* ***93***, pp. 299–314.

[20] Spector, M. J., Guo, Y., Roy, S., Bloomfield, M. O., Maniatty, A., and Mishra, S., 2018. "Passivity-based iterative learning control design for selective laser melting". In 2018 Annual American Control Conference (ACC), IEEE, pp. 5618–5625.

[21] Liao-McPherson, D., Balta, E. C., Wüest, R., Rupenyan, A., and Lygeros, J., 2022. "In-layer thermal control of a multi-layer selective laser melting process". In 2022 European Control Conference (ECC), IEEE, pp. 1678–1683.

[22] Wang, Q., Michaleris, P., Ren, Y., Dickman, C., and Reutzel, E., 2023. "Effect of interlayer temperature on melt-pool morphology in laser powder bed fusion". *Additive Manufacturing Letters,* ***7***, p. 100169.

[23] Kolossov, S., Boillat, E., Glardon, R., Fischer, P., and Locher, M., 2004. "3d fe simulation for temperature evolution in the selective laser sintering process". *International Journal of Machine Tools and Manufacture,* ***44***(2-3), pp. 117–123.

[24] Yin, J., Zhu, H., Ke, L., Lei, W., Dai, C., and Zuo, D., 2012. "Simulation of temperature distribution in single metallic powder layer for laser micro-sintering". *Computational Materials Science,* ***53***(1), pp. 333–339.

[25] Roberts, I., Wang, C., Esterlein, R., Stanford, M., and Mynors, D., 2009. "A three-dimensional finite element analysis of the temperature field during laser melting of metal powders in additive layer manufacturing". *International Journal of Machine Tools and Manufacture,* ***49***(12), pp. 916–923.

[26] Contuzzi, N., Campanelli, S., and Ludovico, A., 2011. "3 d finite element analysis in the selective laser melting process". *International Journal of Simulation Modelling,* ***10***(3), pp. 113–121.

[27] Li, C., Fu, C., Guo, Y., and Fang, F., 2016. "A multiscale modeling approach for fast prediction of part distortion in selective laser melting". *Journal of materials processing technology,* ***229***, pp. 703–712.

[28] Hodge, N., Ferencz, R., and Solberg, J., 2014. "Implementation of a thermomechanical model for the simulation of selective laser melting". *Computational Mechanics,* ***54***(1), pp. 33–51.

[29] Schilp, J., Seidel, C., Krauss, H., and Weirather, J., 2014. "Investigations on temperature fields during laser beam melting by means of process monitoring and multiscale process modelling". *Advances in Mechanical Engineering,* ***6***, p. 217584.

[30] Papadakis, L., Loizou, A., Risse, J., and Schrage, J., 2014. "Numerical computation of component shape distortion manufactured by selective laser melting". *Procedia Cirp,* ***18***, pp. 90–95.

[31] Zaeh, M. F., and Branner, G., 2010. "Investigations on residual stresses and deformations in selective laser melting". *Production Engineering,* ***4***(1), pp. 35–45.

[32] Zhang, W., Tong, M., and Harrison, N. M., 2019. "Resolution, energy and time dependency on layer scaling in finite element modelling of laser beam powder bed fusion additive manufacturing". *Additive Manufacturing,* ***28***, pp. 610–620.

[33] Tran, H.-C., Lo, Y.-L., Le, T.-N., Lau, A. K.-T., and Lin, H.-Y., 2021. "Multi-scale simulation approach for identifying optimal parameters for fabrication ofhigh-density inconel 718 parts using selective laser melting". *Rapid Prototyping Journal.*

[34] Razer, B. *Application Training EOSINT M270Xtended/M280 – EOS 2011 DMLS Technology Principles.* EOS.

[35] Tabor, D., 2000. *The hardness of metals.* Oxford university press.

[36] Kistler, N. A., Nassar, A. R., Reutzel, E. W., Corbin, D. J., and Beese, A. M., 2017. "Effect of directed energy deposition processing parameters on laser deposited inconel® 718: Microstructure, fusion zone morphology, and hardness". *Journal of Laser Applications,* ***29***(2).

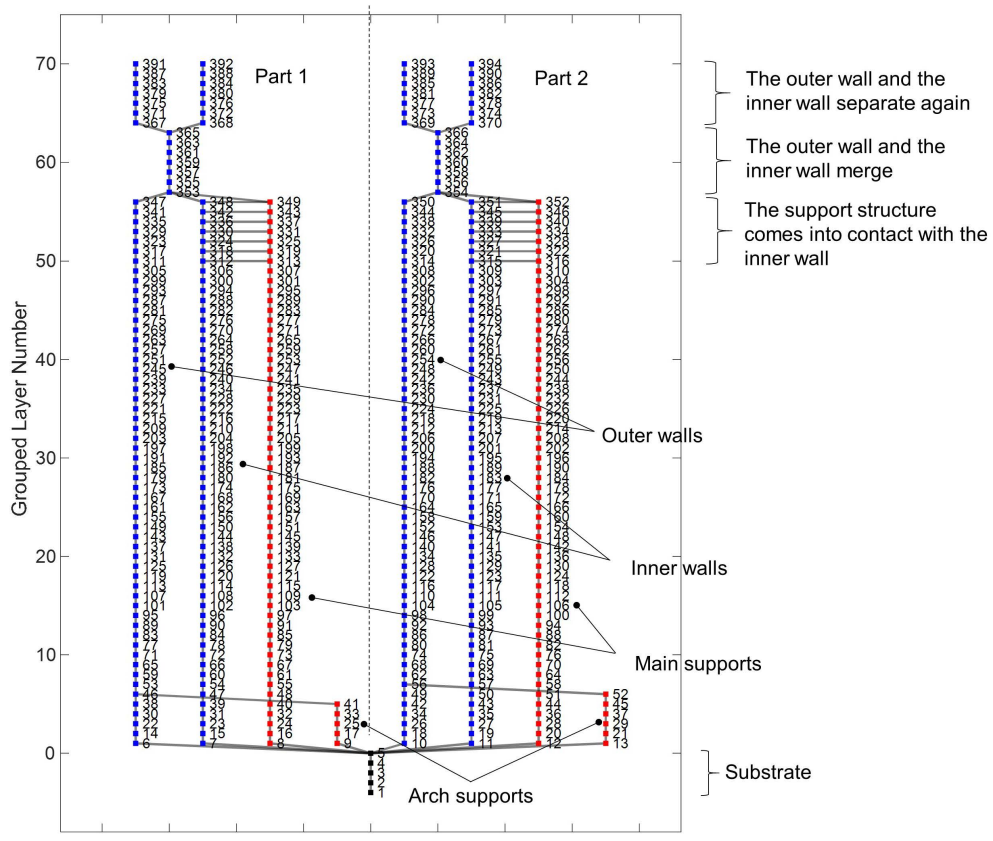

Figure 14: Network structure showing thermal conduction among nodes used in the FD model [19].

Appendix A: Network structure, matrices and thermal parameters of the part-scale thermal model

A network structure showing thermal conduction among the nodes used in the FD model is given in Fig. 14, where powder nodes are not shown for simplicity.

Model matrices Define

$$a_i = \frac{A^i_{cs}\rho_i c_{p,i}\Delta x_i}{\Delta t}, \quad b_{i,j} = \frac{A^{i,j}_{ol}\kappa_{i,j}}{\delta_{i,j}}, \quad c_{i,k} = A^{i,k}_{powd}\gamma_{i,k}, \quad r_i = A^i_{sf}h_i \tag{10}$$

In a_i, A^i_{cs} denotes the cross-sectional area of node i , Δx_i denotes its thickness; ρ_i is its density; $c_{p,i}$ denotes its specific heat. In $b_{i,j}$, $A^{i,j}_{ol}$ denotes the overlap (contacting) cross-sectional area between

node i and its neighboring node j; $\kappa_{i,j}$ denotes the effective thermal conductivity between node i and node j (two nodes could be of different materials); $\delta_{i,j}$ denotes the distance between the centers of nodes i and j. In $c_{i,k}$, $\gamma_{i,k}$ denotes the heat transfer coefficient at the solid-powder interface with $A_{powd}^{i,k}$ denoting the interface area. In r_i, A_{sf}^{i} denotes the surface area of node i exposed to the surroundings, and h_i denotes the surface convection coefficient.

Then, $\mathbf{\Gamma} =$

$$\begin{bmatrix} a_1 + \sum\limits_{j\in\mathcal{N}_1^\ell} b_{1,j} + \sum\limits_{k\in\mathcal{E}_1^\ell} c_{1,k} + r_1 & -b_{1,2} - c_{1,2} & \cdots & -b_{1,N_\ell} - c_{1,N_\ell} \\ -b_{2,1} - c_{2,1} & a_2 + \sum\limits_{j\in\mathcal{N}_2^\ell} b_{2,j} + \sum\limits_{k\in\mathcal{E}_2^\ell} c_{2,k} + r_2 & \cdots & -b_{2,N_\ell} - c_{2,N_\ell} \\ \vdots & \vdots & \ddots & \vdots \\ -b_{N_\ell,1} - c_{N_\ell,1} & -b_{N_\ell,2} - c_{N_\ell,2} & \cdots & a_{N_\ell} + \sum\limits_{j\in\mathcal{N}_{N_\ell}^\ell} b_{N_\ell,j} + \sum\limits_{k\in\mathcal{E}_{N_\ell}^\ell} c_{N_\ell,k} + r_{N_\ell} \end{bmatrix} \tag{11}$$

where $\mathcal{N}_i^\ell$ denote the set of neighboring nodes of node i. When node j represents a solid component, $\mathcal{E}_j^\ell$ represents the set of neighboring powder nodes; when node j represents a powder node, $\mathcal{E}_i^\ell$ represents the set of neighboring solid nodes.

$$\mathbf{\Lambda} = \text{diag}(a_1, \ldots, a_{N_\ell}), \tag{12}$$

$$\mathbf{R} = [r_1, r_2, \ldots, r_{N_\ell}]^\top. \tag{13}$$

Detailed derivations of these matrices are given in [19].

Activation temperature as a function of laser power In the grouped layer ℓ, let $P_\ell^{(i)}$ denote the laser power for node i, and then let $\mathbf{P}_\ell$ denote the resulting vector of laser powers. Let $\mathbf{T}_{act}$ denote the activation temperature vector as a function of $\mathbf{P}_\ell$, where the activation temperature for

node i satisfies

$$T_{act}(P_\ell^{(i)}) = T_a + \frac{\eta P_\ell^{(i)}}{\rho c_p l_{hs} t_\theta v} \tag{14}$$

T_a is the ambient temperature, η is the laser absorption efficiency, l_{hs} denotes the hatch spacing, t_θ is the thickness of each physical layer, and v is the laser scan speed.

Model thermal parameters Model thermal parameters are summarized in Table 6, where only the five parameters (indicated by the prefix $*$) $\kappa_{powd,powd}$, h_{subs}, $h_{powd,side}$, $\gamma_{part,powd}$, and $\gamma_{subs,powd}$ are identified using experimental data. All other thermal parameters are either computed using known material properties or pre-set using past knowledge. In [19], these five thermal parameters were identified using randomly-selected half of the experimental data obtained under the default laser power of 285 W by minimizing the root mean squared error (RMSE) between the model predictions and the measured mean interlayer temperatures. The resulting model was then validated using the other half of the experimental data. In this study where the model is used for control purpose, these five thermal parameters are tuned using the entire set of experimental data obtained under the constant laser power of 285 W and thus their values in Table 6 are slightly different from those in [19].

Table 6: Thermal parameters in the finite-difference model, where $\kappa_{A,B}$ denotes the conduction coefficient between the element type A and B (which can be part, support, substrate, or powder); $\gamma_{C,powder}$ denotes the heat transfer coefficient between the solid component (part/substrate/supp) and powder nodes.

Category	Parameter	Value
Conduction	$\kappa_{part,part}$	0.0114
(W/mmK)	$\kappa_{subs,subs}$	0.0243
	$\kappa_{part,subs}$	0.0078
	$\kappa_{supp,supp}$	0.0031
	$\kappa_{part,supp}$	0.0024
	$\kappa_{subs,supp}$	0.0027
	$*\kappa_{powd,powd}$	1.2×10^{-6}
Convection boundary conditions	h_{top}	1.0×10^{-5}
(W/mm^2K)	$*h_{subs}$	2.1×10^{-5}
	$*h_{powd,side}$	1.0×10^{-6}
Heat transfer between solid and powder elements	$*\gamma_{part,powd}$	3.3×10^{-5}
(W/mm^2K)	$*\gamma_{subs,powd}$	3.3×10^{-5}
	$\gamma_{supp,powd}$	8.4×10^{-6}

$*$: parameters tuned using experimental measurements.

Appendix B: Mean and standard deviation of inner-/outer-wall interlayer temperatures in each grouped layer

Emissivity calibration was conducted in our prior work [3]. The effective emissivity calibration was performed through a dedicated test stand simulating the FLIR position on EOS, where 12 samples were heated to 350 ^oC and then allowed to cool to the room temperature of 22.25 ^oC. Synchronized IR imaging and thermocouple data were recorded during the cool-down period for calibration. More details were given in [3].

Fig. 15 shows the mean and standard deviation of the inner- or outer-wall interlayer temperatures with respect to the grouped layer number. For each grouped layer, under either OPT1 or OPT2, the coefficient of variation (COV) for the inner-wall (or outer-wall) interlayer temperatures is less than 0.086. This is comparable to the interlayer temperature measurements from the uncontrolled sample BL-FullBuild, which has a maximum COV of 0.073.

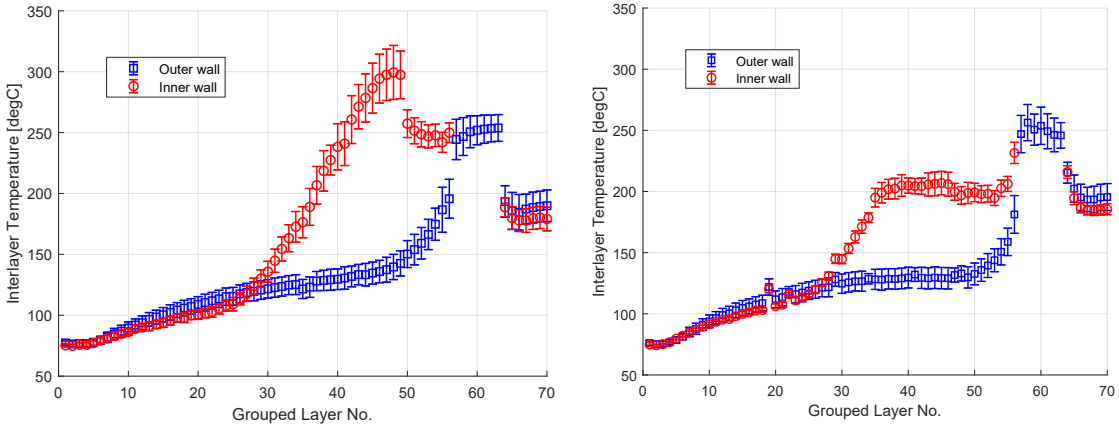

(a) BL-FullBuild

(b) OPT1-FullBuild

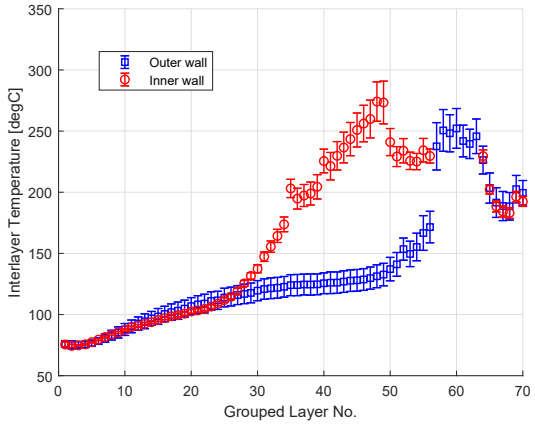

(c) OPT2-FullBuild

Figure 15: Mean and standard deviation of interlayer temperature measurements at each grouped layer, under (a) BL, (b) OPT1, and (c) OPT2.

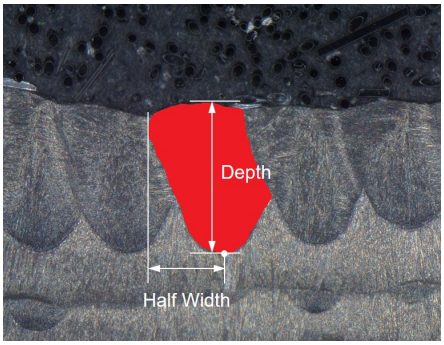

Figure 16: Illustration of melt-pool half-width and melt-pool depth.

Table 7: Mean and standard deviation of melt-pool dimensions under OPT1.

Build	Physical layer No. (interlayer temp, power)	Cross-section	Half-width (μm)	Depth (μm)
OPT1-876	876 (200 ^oC, 150 W)	Mid-of-hatch	63.5±11.9	91.1±20.4
		End-of-hatch	65.4±13.4	93.3±20.4

Appendix C: Melt-pool dimensions from micrograph and melt-pool statistics of OPT1-876

Fig. 16 illustrates how the melt-pool depth and half-width are defined. The melt-pool depth is determined by first identifying the highest and lowest pixels within the melt-pool exposed region, followed by calculating their difference and multiplying by the dimensional scale factor indicated in the legend of the micrograph. The melt-pool half-width is determined as the horizontal distance between the lowest point of the melt-pool and the farthest point on the exposed side of the melt-pool, followed by multiplying the dimensional scale factor.

Although OPT1 has caused lack-of-fusion defects and is excluded from further comparison against OPT2 and BL on micrographs and microhardness, the melt-pool dimensions under OPT1 are given in Table 7 for completeness.